ICANS XIX,
19th meeting on Collaboration of Advanced Neutron Sources
March 8 – 12, 2010
Grindelwald, Switzerland

ENERGY SELECTIVE NEUTRON IMAGING IN MATERIAL RESEARCH

LIDIJA JOSIC, EBERHARD H. LEHMANN, ANDERS KAESTNER
Spallation Neutron Source Division, Paul Scherrer Institut, 5232 Villigen PSI, Switzerland

ABSTRACT

Energy selective neutron imaging is presented as a novel non-destructive method for the analysis of the crystalline structure of bulk samples. It is based on imaging with energy narrowed neutron beams in the low energy range where the total neutron cross sections contain characteristic Bragg edges. We show that the energy selective neutron radiography maps the crystalline structure and determines energy values where the image contrast is the highest. Furthermore, a high contrast neutron tomography visualizes the crystalline structure over the sample volume and enables a three-dimensional inspection that is difficult to perform by other techniques.

1. Introduction

Polychromatic thermal and cold neutron beams are in the standard use for neutron radiography and tomography experiments [1-4] where the image contrast is produced due to the attenuation of the initial neutron beam by the sample. Attenuation is the unique property of the material through the energy averaged total neutron cross section that enables an analysis of the sample structure and composition. In the cold range, the image contrast is more pronounced because of the higher energy averaged cross sections that attenuates the initial beam more effectively in comparison to the thermal range. Although having the advantage of high neutron fluxes and thus low exposure times, in polychromatic neutron imaging the energy dependent characteristics of the sample are not visible. Narrowing the energy band increases the image contrast significantly, especially for polycrystalline materials in the cold energy range where the total neutron cross sections show characteristic Bragg edges (Fig. 1). In general, the image contrast is produced by choosing the energy where the attenuations of different materials differ.

Energy selective neutron imaging in the cold energy range has been firstly performed by applying a velocity selector device in both radiography and tomography modes [5-7]. Further improvements in the energy resolution have been achieved at the CONRAD cold neutron beam line of Helmholtz Zentrum Berlin (HZB) [8] by an installation of a double monocrystal monochromator and at ICON cold neutron beam line of Paul Scherrer Institut (PSI) [2] by using a velocity selector of a higher performance. The first experiments that managed to image the crystalline structure of single component samples have been performed at ICON and later confirmed in experiments at ISIS pulsed source [9]. The temporal and spatial resolutions were high enough to detect the presence of textures in the radiography mode. In this work, results of the latest simultaneous improvement in energy and spatial resolutions applied to the analysis of the crystalline structure in the welded stainless steel sample are presented. For the first time, the crystalline structure has been visualized in three dimensions by performing the energy selective neutron tomography.

2. Neutron Cross Sections and Transmission

When a neutron interacts with an atom, it can be either absorbed or dominantly scattered by the atomic nucleus. If neutrons interact with materials, the total cross section $\sigma(\lambda)$ consists of elastic and inelastic coherent and incoherent scattering components and absorption [10]. In particular, only the elastic coherent component includes the structural parameters while the others either continuously increase or decrease with λ. It can be seen, for example, in the resolved total cross section of Pb [11] or Fe (fcc) (Fig. 1, right).

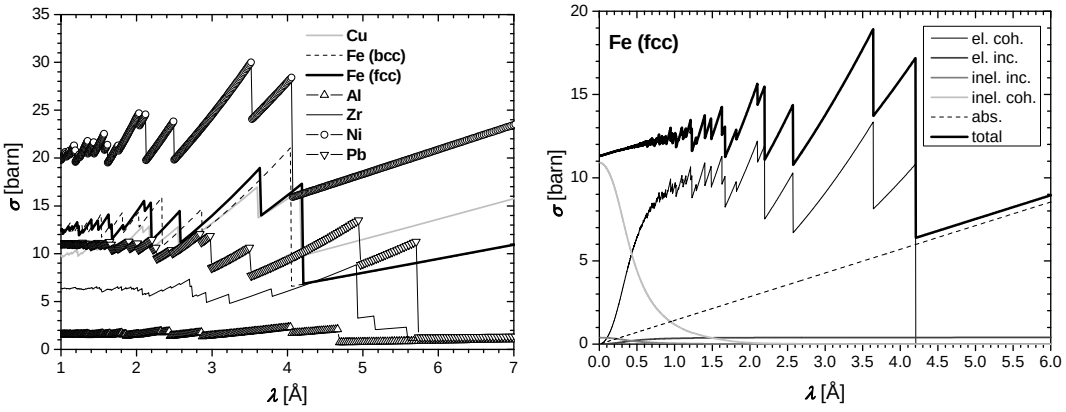

Fig. 1. Left: Total neutron cross sections (σ) for seven different polycrystalline materials derived from the CRIPO code [12]. Right: Total neutron cross section (total) and its components: elastic and inelastic coherent and incoherent (el. coh., inel. coh., el. inc., inel. inc.) and absorption for Fe (fcc). Elastic coherent scattering with characteristic peaks and Bragg edges enables a contrast change in the energy selective neutron imaging.

For any type of the perfect structure, the elastic coherent scattering cross section is given by [13, 14]:

$$\sigma_{coh}^{el}(\lambda) = \frac{\lambda^2}{2V_0} \sum_{d_{\boldsymbol{h}}=0}^{2d_{\boldsymbol{h}}<\lambda} |F_{\boldsymbol{h}}|^2 d_{\boldsymbol{h}} \tag{1}$$

where V_0 is the volume of the unit cell, $F_{\boldsymbol{h}}$ the structure factor [10], $\boldsymbol{h}$ the reciprocal vector and $d_{\boldsymbol{h}} = 1/h$ the spacing of the particular set of crystallographic planes (h, k, l). It can be shown that a significant scattering intensity is obtained only if the neutrons are scattered coherently. This is fulfilled if the Bragg law:

$$2d_{hkl} \sin\theta = \lambda \tag{2}$$

is valid, where θ is the scattering angle. In our image interpretation, we can directly make use of this Bragg law relation in the both qualitative and quantitative manners for the first time. In neutron transmission experiments and thus imaging, crystallographic parameters are obtained by an analysis of the measured transmission patterns. Those patterns show a set of peaks superimposed to the continual background. According to the Bragg law, Eq. 2, different sets of crystallographic planes contribute to the transmission pattern and each single (h, k, l) set only in the wavelength range from $\lambda = 0$ to $\lambda = 2d_{hkl} = \lambda^{max}$. λ^{max} is named the Bragg edge or Bragg cut off because above that value reflections from a

corresponding (h, k, l) set are not anymore possible. Consequently, a sharp increase in the transmission appears at each λ^{max} value. If the sample is a powder or a polycrystal with randomly orientated crystallites, the transmission between Bragg edges is continual. In the quantification sense, the height of the (h, k, l) Bragg edge provides a number of crystallites with the (h, k, l) plane perpendicular to the incident neutron beam direction and the transmission left from the Bragg edge in the wavelength scale, the number of crystallites with possible (h, k, l) reflections under the angle:

$$\alpha_{hkl} = \frac{\pi}{2} - \arcsin\left(\frac{\lambda}{2d_{hkl}}\right). \tag{3}$$

Finally, the Bragg edge position on the wavelength scale determines the lattice spacing $d_{hkl} = \lambda^{max}/2$.

3. Neutron Imaging Experiment

In neutron imaging the standard experimental set-up consists of the neutron source, sample and neutron 2D detector positioned perpendicular to the source-sample direction. In ideal experimental conditions, only those neutrons that were transmitted through the sample reach the detector while neutrons absorbed or scattered by the sample are removed from the incident neutron beam. From the detector side several solutions are in the standard use [15, 16]. In order to be detected, neutrons are firstly absorbed by one of the most common isotopes B-10, Gd or Li-6 and produced secondary ionizing radiation is effectively detected. Described set-ups are currently adopted on the available imaging beam lines and the layout of the ICON cold neutron imaging beam line of Paul Scherrer Institut is shown in Fig. 2 (left).

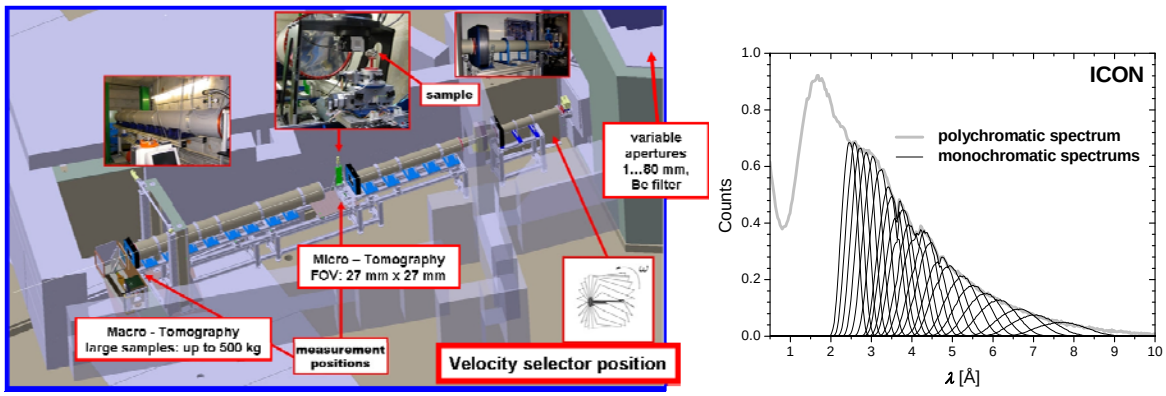

Fig. 2. Left: Layout of the cold neutron imaging beam line – ICON of Paul Scherrer Institut. Right: polychromatic (thick gray line) and monochromatic (black lines) energy spectrums. Velocity selector device was used to select monochromatic neutron beams from the initially polychromatic neutron source.

To select monochromatic neutron beams from the initially polychromatic neutron source either a velocity selector device or double monocrystal monochromators are in use. Velocity selector is made of absorbing helical blades inserted in the rotor with the changeable rotation frequency and acts as a moving collimator in the wavelength space (Fig. 3, left). Only neutrons that manage to pass between the blades, in the time interval

determined by the rotation frequency, are transmitted and contribute to the narrowed wavelength distribution.. In double monocrystal monochromators (Fig. 3, right), the monocrystals are rotated according to the Bragg law and reflected neutrons form the wanted wavelength band.

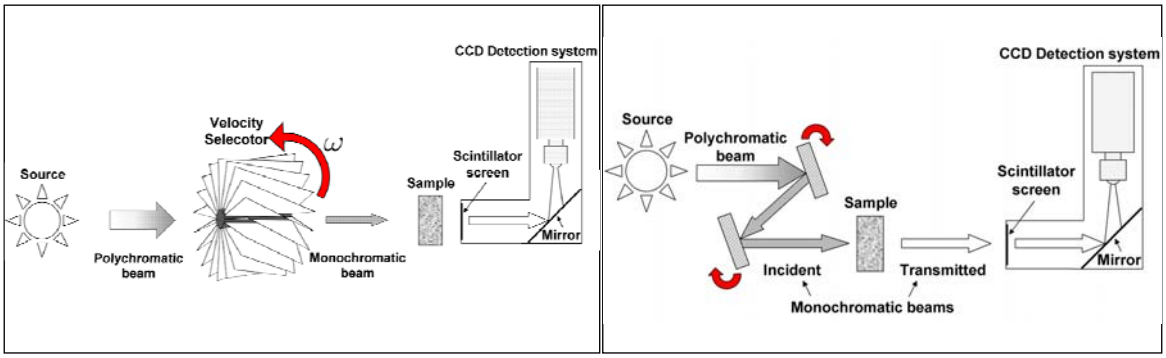

Fig. 3. Schematic drawings of neutron imaging beam lines for energy selective neutron imaging. Monochromatic neutron beams are extracted from the initially polychromatic neutron source either with a velocity selector device (left) or a double monocrystal monochromator (right).

The measurable quantity in the neutron imaging experiment is the neutron beam intensity behind the sample $I(x, y)$ for each detector pixel (x, y) weighted by the energy depended detector efficiency ε and averaged over the neutron energy spectrum at the detector position and over the sample thickness in the beam direction (z). According to the exponential attenuation law, $I(x, y)$ can be evaluated as:

$$I(x,y) = \int I_0(x,y,E)\varepsilon(E)\exp\left(-\int \Sigma(x,y,z,E)dz\right)dE \qquad (4)$$

where $\Sigma(x, y, z, E) = n(x, y, z)\cdot\sigma(E)$ is the attenuation coefficient, $n(x, y, z)$ the number of sample atoms per unit volume, $\sigma(E)$ the total neutron cross section and E the neutron energy ($E = h^2/(2m_n\lambda^2)$, h – Planck's constant, m_n – neutron mass). Measuring the beam intensity without the sample in the beam $I_0(x, y)$, transmission is readily obtained as a ratio $T(x, y) = I(x, y)/I_0(x, y)$. This further enables an evaluation of the attenuation coefficient $\Sigma = -\ln(T(x, y))/z$ averaged over the energy spectrum and sample thickness z.

Several effects can disturb the pure transmission signal. The dominant one is a detection of not only transmitted neutrons but also neutrons scattered from the sample at small sample-detector distances [17, 18]. This means that total cross sections need to be well determined in order to subtract the scattering component from the radiograph. Numerical procedures based on Monte Carlo simulations of the neutron radiography experiment are usually used for an estimate of the scattering component by using analytically evaluated cross sections as an input [19, 20]. After the correction, the pure transmission image is obtained which provides the full image contrast.

4. Experimental Results and Interpretation

Energy selective neutron radiography and tomography experiments were performed at two cold neutron imaging beam lines: ICON and CONRAD. Velocity selector employed at ICON provided wavelength bands widths of $\Delta\lambda/\lambda \sim 0.15$ and a double monocrystal monochromator at CONRAD the wavelength bands in the range $0.1 > \Delta\lambda/\lambda > 0.01$. At the

both beam lines the same detection system developed at PSI was used, consisted of the cooled CCD camera with the 13.5 μm pixel size and neutron absorbing Gd and Li scintillators that in combination with a good quality of the neutron beams (collimation, size, homogeneity and divergence) assured the spatial resolution of ~50 μm. The aim of the experiments was to derive total neutron cross sections for different polycrystalline materials and to visualize and quantify the energy and spatially resolved structural parameters of the complex material structure such welded stainless steel entirely by neutron imaging.

Transmission through polycrystalline plates of different thicknesses was measured in the broad wavelength range between 2.0 and 6.0 Å in 0.05 Å steps at CONRAD and at six wavelengths at ICON. Attenuation coefficients Σ were evaluated from corrected radiographs and compared to analytically evaluated values obtained with the CRIPO code [12]. Results for Pb, Zr and Ni are shown in Fig. 4 as examples. Experimental values from both ICON and CONRAD beam lines agree well while the large differences exist in comparison to the CRIPO data in some wavelength ranges. This indicates the presence of textures in the measured samples that are especially strong in Pb, with the complete absence of the first Bragg edge, and that the scattering contribution to the radiographs needs to be subtracted which was confirmed for the case of Al [21]. With this experiment, it is shown that neutron imaging can provide structural parameters of crystalline materials (Bragg edges positions).

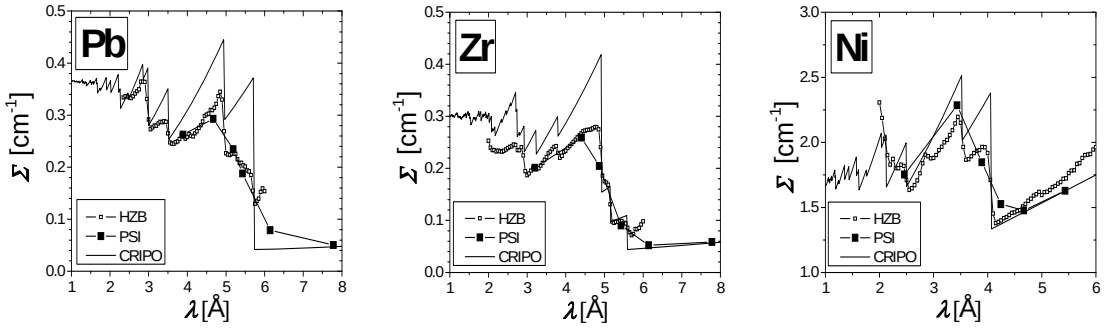

Fig. 4. Neutron attenuation coefficients (Σ) for Pb, Zr and Ni polycrystalline materials obtained experimentally at ICON, PSI (solid symbols) and CONRAD, HZB (open symbols) compared to the analytically evaluated data (CRIPO code [12], solid lines).

Experiments with a stainless steel weld [22] were performed in both energy selective radiography and tomography modes. A radiography energy scan was made in the wavelength range between 3.0 and 6.0 Å with a wavelength step of 0.1 Å at CONRAD, HZB using a detection system from ICON, PSI. The imaged region of the sample includes the weld and the bulk material from the both side of the joint area. Σ values were evaluated for a weld thickness of 20 mm in the beam direction and for each pixel, the most probable Σ value in a Gaussian like distribution has been chosen as representative. Maps of Σ values measured at 3.5 Å, 4.1 Å and 5.1 Å are shown in Fig. 5. It can be immediately seen that long thin vertical stripes are visualized for each energy except 5.1 Å. Those imaged structures are perpendicular to the direction of the welding line, which can be seen from the comparison with the image taken by the standard optical microscopy of the polished and etched sample surface (Fig. 6). Further, the image contrast converts over the energy range with the highest contrast difference between images at 3.5 Å and 4.1Å while at 5.1 Å the image contrast vanishes.

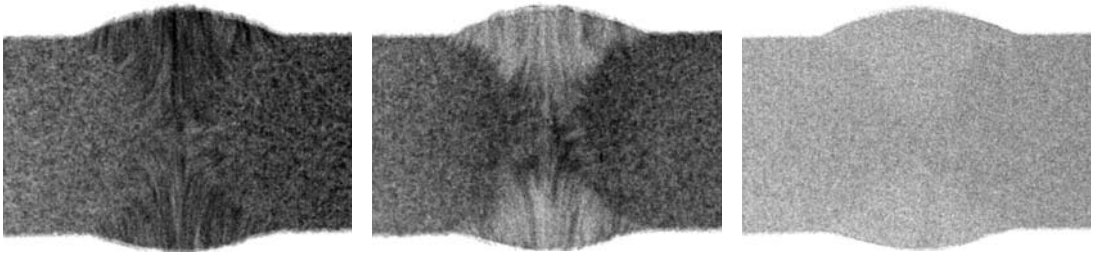

Fig. 5. Radiography images of the welded stainless steel sample at 3.5 Å, 4.1 Å and 5.1 Å.

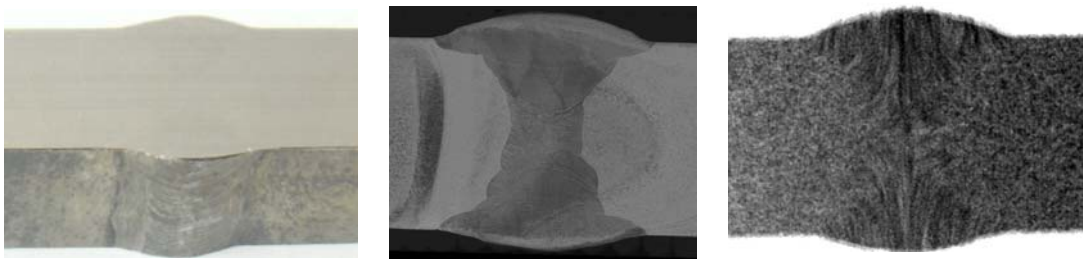

Fig. 6. Photo image (left), optical microscopy image (middle) and radiography image at 3.5 Å (right) of the welded stainless steel sample.

The obtained maps of Σ values over the weld area can be interpreted by the presence of different crystallographic textures in different weld regions. Each texture has a preferred direction in respect to the incident beam direction and thus attenuates the beam differently, which in turn changes the image contrast. For example, the energy dependence of Σ for three different regions 1, 2 and bulk can be analyzed (Fig. 7). Region 1 follows one stripe of the welded zone, region 2 the second with the opposite contrast and a bulk region the zone of the sample not affected by the welding process. It can be seen that regions 1 and 2 show the opposite Σ curves with peaks at 3.5 Å and 4.1 Å. This explains the opposite contrast on the images at 3.5 Å and 4.1 Å. Because at 4.1 Å only reflections from (111) planes of the stainless steel are possible (the first Bragg edge is at 4.169 Å and the second at 3.6105 Å, [9]), according to Eq. 3, the peak at 4.1 Å corresponds to the preferred orientation of (111) planes in the region 1 at an angle of ~ 10^{o} in respect to the incident beam direction. The region 2 contains both, (111) planes with an orientation at an angle of ~ 33^{o} and (200) planes at an angle ~ 14^{o} because the peak in Σ energy dependence at 3.5 Å lies below the second Bragg edge and reflections from (200) planes become also possible. The bulk region does not show pronounced peaks in the Σ distribution that correspond to the randomly orientated crystallites in the zone not affected by the welding process. A radiography image at 5.1 Å shows no contrast because the scattering is not possible in the absorption energy range (above the first Bragg edge at 4.169 Å in the wavelength scale). Those results show that the energy selective neutron imaging provides an insight into the crystallographic structure of materials.

To verify the presence of textures in the welded zone of the sample in three dimensions, energy selective tomographies were performed at 3.5 Å and 4.1 Å. A tomography run in the polychromatic beam was performed as a reference. It is shown that reconstructed slices from the middle of the sample (Fig. 8, left) as well the reconstructed

volumes (Fig. 8, right) visualize textures in the weld at 3.5 Å and 4.1 Å and that textures can not be visualized in the polychromatic beam.

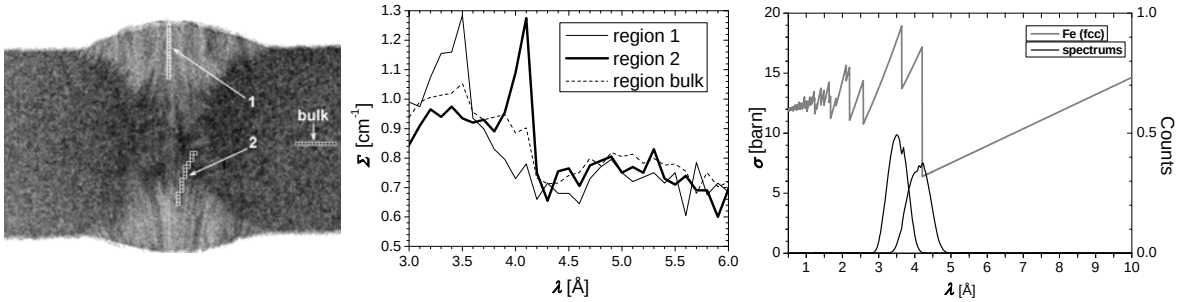

Fig. 7. Energy selective radiography of the welded stainless steel sample. Left: Radiograhy image at 4.1 Å with marked regions: 1, 2 and bulk. Middle: Most probable values of attenuation coefficients (Σ) over the wavelength range: 3.0 Å – 6.0 Å for 1, 2 and bulk regions. Right: Total neutron cross section for Fe (fcc) and energy spectrums at 3.5 Å and 4.1 Å peak positions.

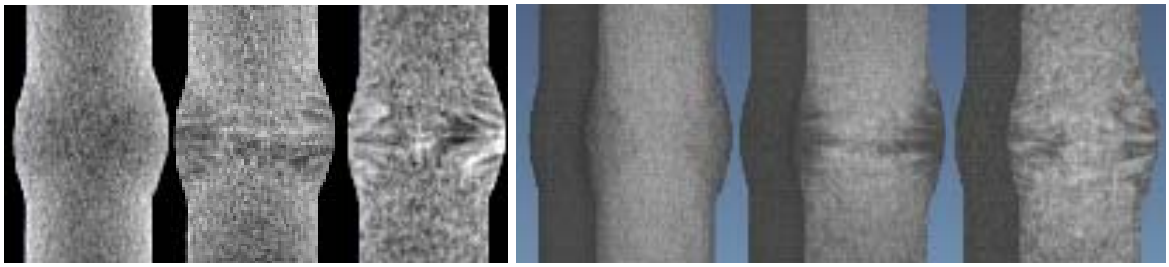

Fig. 8. Energy selective tomography of the welded stainless steel sample. Left: Reconstructed slices from the bulk of the sample in the polychromatic beam (left), at 4.1 Å (middle) and at 3.5 Å (right). Right: Reconstructed volumes in the polychromatic beam (left), at 4.1 Å (middle) and at 3.5 Å (right).

5. Conclusion

The presented work shows that the energy selective neutron imaging enables a determination of the crystalline structure in engineering materials such welds and provides both: visualized and quantified maps of structural parameters over the large sample area and thickness. It is envisaged that the method will be employed in various industrial applications and developed towards improved energy and spatial resolutions.

Acknowledgments

The authors gratefully acknowledge Dr. Nikolay Kardjilov and his team from Helmholtz-Zentrum, Berlin (HZB), Germany (former Hahn-Meitner Institut, Berlin, Germany) for fruitful collaborations and granting us the beam time at CONRAD cold neutron imaging beam line.

6. References

1. P. Vontobel, E. H. Lehmann, R. Hassanein, and G. Frei, *Physica B* **385–386** (2006) 475.

2. G. Kühne, G. Frei, E. Lehmann, P. Vontobel, A. Bollhalder, U. Filges, and M. Schild, *Swiss Neutron News* **28** (2005) 20.
3. N. Kardjilov, A. Hilger, I. Manke, M. Strobl, W. Treimer, and J. Banhart, *Nuclear Instruments and Methods in Physics Research A* **542** (2005) 16.
4. B. Schillinger, J. Brunner, and E. Calzada, *Physica B* **385–386** (2006) 921.
5. S. Baechler, N. Kardjilov, M. Dieric, J. Jolie, G. Kühne, E. Lehmann, and T. Materna, *Nuclear Instruments and Methods in Physics Research A* **491** (2002) 481.
6. N. Kardjilov, S. Baechler, M. Bastürk, M. Dierick, J. Jolie, E. Lehmann, T. Materna, B. Schillinger, and P. Vontobel, *Nuclear Instruments and Methods in Physics Research A* **501** (2003) 536.
7. N. Kardjilov, B. Schillinger, and E. Steichele, *Applied Radiation and Isotopes* **61** (2004) 455.
8. W. Treimer, M. Strobl, N. Kardjilov, A. Hilger, and I. Manke, *Applied Physics Letters* **89** (2006) 203504.
9. W. Kockelmann, G. Frei, E. H. Lehmann, P. Vontobel, and J. R. Santisteban, *Nuclear Instruments and Methods in Physics Research A* **578** (2007) 421.
10. S. Vogel, *A Rietveld-Approach for the Analysis of Neutron Time-Of-Flight Transmission Data* (Dissertation, Uni. Kiel, 2000).
11. G. Muhrer, T. Hill, F. Tovesson, and E. Pitcher, *Nuclear Instruments and Methods in Physics Research A* **572** (2007) 866.
12. F. Kropff and J. R. Granada, *CRIPO: A fast computer code for the evaluation of σ_T in Polycrystalline materials*, unpublished Report (CAB-1977).
13. S. W. Lovesey, *Theory of neutron scattering from condensed matter, Volume 1: Nuclear scattering* (Clarendon Press, Oxford, 1986).
14. J. R. Granada, *Z. Naturforsch.* **39a** (1984) 1160.
15. E. H. Lehmann, P. Vontobel, G. Frei, and C. Brönnimann, *Nuclear Instruments and Methods in Physics Research A* **531** (2004) 228.
16. E. Lehmann and P. Vontobel, *Applied Radiation and Isotopes* **61** (2004) 567.
17. N. Kardjilov, F. de Beer, R. Hassanein, E. Lehmann, and P. Vontobel, *Nuclear Instruments and Methods in Physics Research A* **542** (2005) 336.
18. R. Hassanein, E. Lehmann, and P. Vontobel, *Nuclear Instruments and Methods in Physics Research A* **542** (2005) 353.
19. R. Hassanein, *Development of correction algorithm to approach quantitative neutron tomography* (Dissertation, ETHZ, 2006).
20. D.B. Pelowitz (Ed.), *MCNPX User's Manual* (Version 2.5.0, LA-CP-05-0369, Los Alamos National Laboratory, April 2005).
21. L. Josic, E.H. Lehmann, G. Frei, and M. Tamaki, *Nuclear Instruments and Methods in Physics Research A* **605** (2009) 21.
22. R. Stoenescu, *Effects of neutron irradiation on the microstructure and mechanical properties of the heat affected zone of stainless steel welds* (Dissertation, EPFL, 2005).